stellarator news

An international journal of news from the stellarator community

Editor: James A. Rome Issue 157 June 2017
E-Mail: James.Rome@stelnews.info Phone: +1 (865) 482-5643
On the Web at https://stelnews.info

Letter from the Editor: *Stellarator News* has moved

Stellarator News (SN) began sometime before 1988 as "A compendium of news, proposals, progress, and people in the international stellarator community." It was started by the Fusion Energy Division of Oak Ridge National Laboratory (ORNL) and hosted by ORNL for many years. However, due to increased computer security at ORNL, beginning in May 2017, I have moved SN to https://stelnews.info, and am publishing SN independently.

SN has been published electronically every other month when there are available contributions. As Editor, I assemble, vet, clarify meaning, and format the content. The English (and often the meaning) is professionally edited by Margaret B. (Bonnie) Nestor. Her incredible editing is a great reason to submit prepublication works to SN, even if English is your native language. Rapid publication (a few weeks from the due dates for issue submission) is a hallmark of this publication.

SN accepts articles about theory, experiment, engineering, proposals, and politics of relevance to the stellarator community. Speculative works are welcomed, and the more pretty color pictures that explain the content, the better. Authors should try to make their submissions intelligible to the non-specialist.

Stellarator News serves multiple purposes:

⇨ Primarily it serves to coordinate efforts among the worldwide stellarator researchers. SN provides an opportunity to quickly convey information to the stellarator community. It also publicizes meetings, such as the International Stellarator Workshops and the Coordinated Working Group Meetings, and publishes their conclusions. In contrast to tokamaks (which have just a handful of adjustable design parameters), there is a wide variety of different viable stellarator concepts, and their design, construction, engineering, and performance are discussed herein with a view towards coordinating and reducing duplication of effort.

⇨ SN informs other interested parties (other branches of fusion research, program managers, elected officials) about the above efforts to showcase the strength and vibrancy of our community.

On the new Web site, I have scanned in the oldest issues that were heretofore unavailable, and used OCR to make all issues searchable, albeit in a kludgey way. Read the instructions to get this feature to work. As always, the "In this issue..." box will appear if you hover over the issue name

SN is published in February, April, June. August, October, and December. Submissions are due by the end of the preceding month. Please send submissions to the Editor at James.Rome@stelnews.info. Be sure to include a short (few sentence) abstract for the "In this Issue" box on the front page, and provide the author's contact information.

James A. Rome, Editor of *Stellarator News*
E-mail: James.Rome@stelnews.info

In this Issue . . .

The bolometer diagnostic at Wendelstein 7-X and its first results from the initial campaign

Introduction

In view of the intrinsic three-dimensionality of Wendelstein 7-X (W7-X), a multicamera bolometer system has been planned to diagnose the radiation loss distribution. The whole system consists of three subsystems — a bulk bolometer system, a divertor bolometer system, and a supplementary system dedicated to 3D effects. According to their respective functions, they are positioned at appropriate poloidal and toroidal locations between a triangular and a bean-shaped plane, covering almost one complete half of a field period [1]. The three subsystems will be installed sequentially on the machine, following a sequence according to the expected plasma scenarios and the experimental programs.

For the first ten-week experimental campaign started on 10 December 2015 [2], two bolometer cameras had been installed on a triangular plane to measure the bulk plasma radiation. The plasmas were operated with five inboard carbon limiters, and heated by electron cyclotron resonant heating (ECRH) with a total maximum heating power of about 4 MW. A maximum central $T_e(0)$ = 8 keV and $T_i(0)$ = 2 keV have been achieved and the line-integrated density $\langle n_e \rangle$ was typically less than 3×10^{19} m^{-2}. During this campaign, the design functions of all bolometer components were checked and verified step by step. The sensitivity of the resistive bolometer detectors, which were originally optimized for higher radiation intensities of high-performance plasmas, had to be re-optimized for the low-density and low-heating-power limiter plasmas.

Diagnostic arrangements

The bolometer system in the first campaign consists of two cameras with carefully constructed arrays of Au-foil resistive detectors [3,4] — a horizontal bolometer camera (HBC) with 32 channels and a vertical bolometer camera (VBC) with two detector arrays of 24 channels each. The detectors have a high responsivity to plasma radiation in the VUV and soft-X range (300 nm–0.2 nm). They were calibrated via an in situ Ohmic heating method [3] and provide line-integrated signals. Figure 1 shows the positions of the two cameras on W7-X and their lines of sight (LoS). The LoS of the HBC span the whole cross-section of the vacuum vessel, thus guaranteeing complete coverage of the plasma cross section including the limiter scrape-off layer. The horizontal elongation of the plasma cross section at the triangular plane requires a larger viewing angle for the VBC. This is realized by integrating two separate detector arrays in this camera, with each having its own aperture and orientation. Due to the limited port space, the LoS have to be designed in a fan-shape and all detectors (4-channel bolometer heads) have the same distance to the aperture center in order to reduce the optic incident angles and hence to achieve a maximum power flux reception.

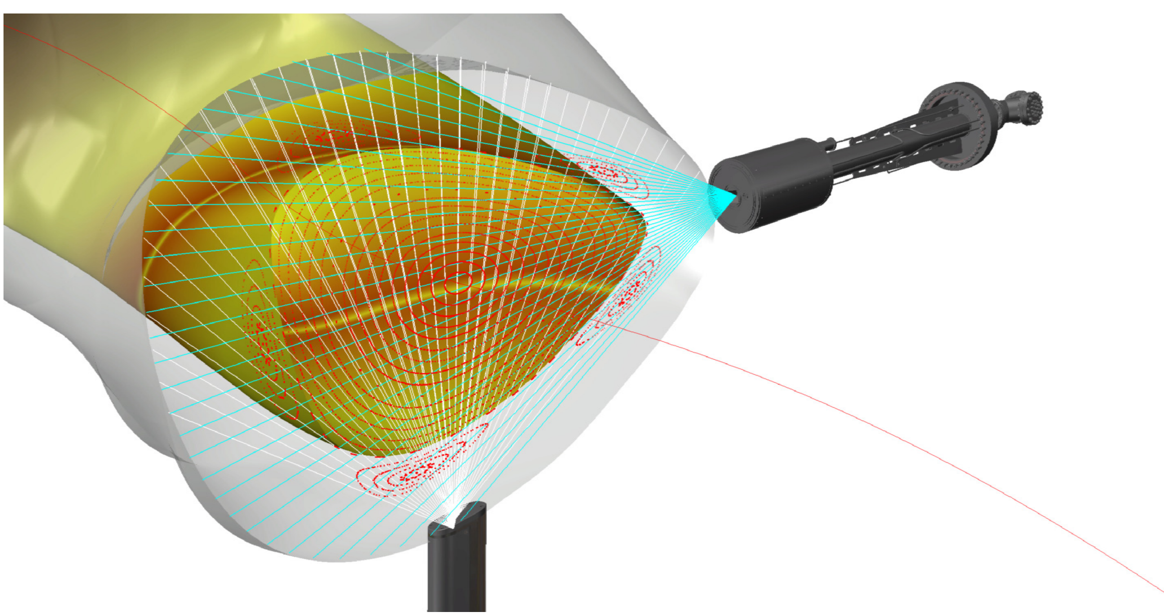

Fig.1. Setup of two bolometer cameras on W7-X viewing the plasma at the triangular cross section. The horizontal bolometer (HBC) has 32 channels and the vertical one (VBC) consists of two sub-cameras with 24 channels each.

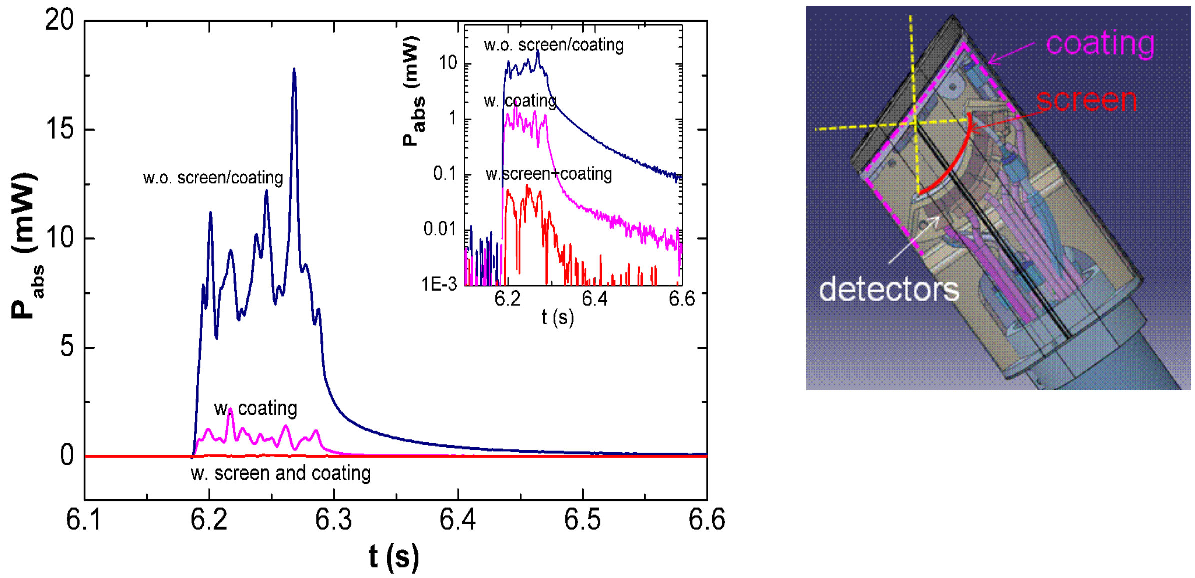

Fig. 2. Left: Test results of a bolometer prototype in a strong microwave background provided by MISTRAL in cases with and without microwave suppression measures. A microwave absorber coating leads to a reduction of the microwave impact by a factor of 10. A further reduction by a factor of 30 is achieved by using a metal mesh in front of the detectors. Right: The location of the metal mesh screen and the ceramic coating in the design of the vertical bolometer camera.

Because the metal-foil resistive bolometer also absorbs microwave radiation, despite a low absorption coefficient (0.1–1.0% depending on the roughness and the oxidation of the surface), sufficient screening of the cameras from microwave stray radiation is one of the most critical issues in the bolometer design. Two technical solutions have been found. First, a metal mesh (made of stainless steel) with an opening smaller than half of the microwave wave length is mounted in front of the detector array for microwave screening. With a wire diameter of $\phi = 90$ μm and an opening of $w = 0.24$ mm, the metal mesh has a sufficiently small microwave transmission factor of ~5%, while keeping an acceptably high optic transmission factor of about 53%. Second, the inner surface of the detector housing is coated by a microwave absorbing ceramic layer (TiO/Al_2O_3) to reduce multi-path reflectance of the microwaves coming into the camera housing. The efficiencies of these techniques have been tested using a prototype of the W7-X bolometer in a strong microwave background provided by the MISTRAL chamber [6, 7]. The experimental results are shown in Fig. 2. The ceramic coating led to a reduction of the microwave impact by a factor of 10, which is further suppressed by a factor of about 30 by the mesh screen. For the W7-X bolometer in use, additional Cu-Be springs are

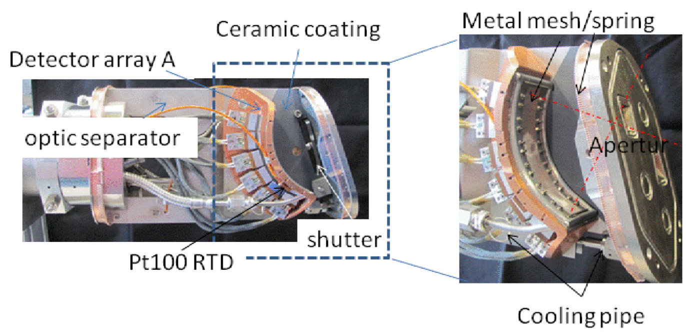

Fig. 3. The structure of the camera head of the vertical bolometer. Two detector arrays are separated by an optic separator, with a metal mesh mounted in front of the detector array for microwave screening. A Cu-Be spring welded on the aperture holder is used as microwave sealing between the detector holder and the housing; the optic separator and the detector enclosures (not shown) are coated with a ceramic TiO/Al_2O_3 layer for absorbing stray microwave radiation.

welded on the aperture holder to avoid microwave leakage between the detector holder and the housing, as shown in Fig. 3. For the purely ECR-heated plasmas during the whole first experiment phase, no microwave perturbations could be detected by the bolometer.

A UHV-compatible pneumatic-driven shutter has been designed and implemented in the bolometer system. Remote control of the shutter, which is necessary because of restricted accessibility to the diagnostics during experiments. was successfully demonstrated. In the first experimental campaign, this shutter was used to protect the detectors against contamination during wall conditioning procedures. For the later long-pulse discharges in W7-X, closure of the shutter allows researchers to perform in situ calibration and to turn off measurement between experiment segments.

In order to limit the smear-out effect originating from the intersections of the LoS with the 3D flux surfaces in W7-X, the toroidal extension of the lines of sight are restricted in such a way that the displacement of the magnetic axis is smaller than the spatial resolution in the poloidal cross section. Thus, the toroidal dimension of the slit aperture is associated with the required spatial resolution and signal/noise ratio. The expected signal/noise ratio on average for most plasma conditions of interest, e.g., for 10 MW ECRH power, is larger than 500. The electronic system has a noise level that corresponds to a signal induced by an absorbed power of ~ 200 nW.

The W7-X bolometer system was designed with features meeting the W7-X steady-state operation requirements [5]. Some technical aspects relevant to long pulses (ten minutes or longer) and high heating powers, e.g., thermal drift suppression/correction, could not yet be assessed in the first campaign.

First experimental results

Time traces of P_{rad} and plasma parameters

During the first experimental campaign, discharges were usually terminated in one of two ways: (1) turn-off of heating constrained by the total input energy limit of 4 MJ due to still incomplete shielding and hardening of in-vessel components in this first campaign, and (2) radiative collapse (RC) due to enhanced impurity radiation. It has been observed by spectroscopic diagnostic (HEXOS) [7] and pulse height analysis (PHA) [8] that the main intrinsic impurity species in the plasma are carbon and oxygen, followed by traces of chlorine, sulfur, fluorine, copper, and occasionally iron.

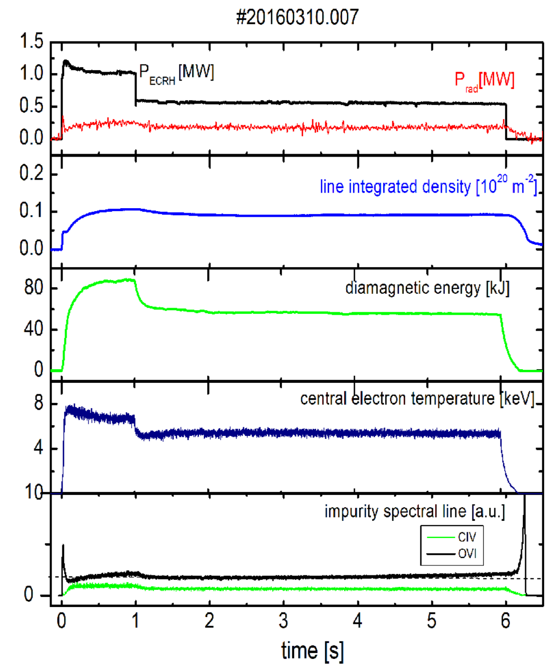

Fig. 4. Time traces for a long (6 s) hydrogen discharge. Shown are (from top to bottom) the ECRH power, the total radiative power loss, the line-integrated plasma density, the diamagnetic energy, the central electron temperature, and spectroscopy signals from C IV and O VI.

Usually, after 20–40 min glow discharge conditioning, stationary plasma density could be maintained and long discharge duration became possible. Figure 4 shows the time traces of a 6-s-long H_2 discharge (#20160310.007). The discharge was started with 1 MW of ECRH power [9], which is later reduced to 0.6 MW in order to limit the total injected energy to below 4 MJ. The plasma was maintained in a stable state and actively terminated after the 4 MJ input energy limit was reached. The central electron temperature $T_e(0)$ measured by the Electron Cyclotron Emission (ECE) diagnostic [10] reached 5 keV at a line-integrated density, measured by a dispersion interferometer [11], of around 1×10^{19} m^{-2}. The diamagnetic energy measured by a diamagnetic loop [12] was ~60 kJ. The total radiated power P_{rad}, estimated by linearly volume-scaling the bolometer signals under the assumption of toroidal symmetric radiation, is around 150 kW, i.e., about 25% of the 600 kW heating power. Line radiations from C IV and O VI measured by HEXOS are shown in the lowest panel of Fig. 4. It is noteworthy that, in a later phase after turn-off of the ECRH, the O VI emission rises sharply, while the C IV emission decreases gradually. The bolometer measurements correlate more closely to the time traces of the carbon impurities in this decay phase, indicating that carbon could be the major radiator in this discharge. After wall conditioning, oxygen concentration should be low, thus making less contribution to the total plasma radiation.

Figure 5 shows another typical H_2 discharge (#20160310.011), which was terminated by RC. The discharge was started with 2 MW of heating power, which was increased to 3.8 MW with a simultaneous hydrogen gas puff at a later time point ($t = 0.3$ s). The plasma density rose continuously before the second gas puff ($t = 0.3$ s) occurred, probably because of outgassing from limiters or wall elements [13]. The energy confinement (diamagnetic energy) improved continuously until a third gas puff at $t = 0.65$ s driving the plasma into a thermally unstable state (see the evolution of P_{rad}). The central T_e reached 8 keV and doesn't change very much during the discharge, while the edge ECE channels ($\rho = 0.8$) detect a clear drop of T_e at the edge after the sharp rise of P_{rad}. The radiation fraction increases from 22% in the 2 MW heating power case up to ~37% before the thermal instability ($t \sim 0.65$ s). The spectral lines of C IV (31nm) and O V (76nm), and the bolometer channel signals (ch17 through $\rho = 0$ and ch9 through $\rho = 0.75$) are shown in the last two panels. The O V-emission measurement clearly demonstrates the importance of oxygen in contributing to this radiation enhancement. The C IV emission level is maintained despite the edge temperature change at $t = 0.3$ s, implying that the C-ion emission zone lies outside this region, i.e., closer to the limiters ($\rho \sim 1$).

The bolometer measurements were in accordance with the ECE results: the enhanced radiation, after gas puffing, originates at the edge where the temperature dropped. The third H_2 puff at $t = 0.65$ s results in rapid increment of the plasma density, accompanied with sharp increases of all the radiation/emission related diagnostic signals collected in Fig. 5. After this time point, the plasma develops into a thermally unstable state (RC) in the sense that P_{rad} quickly reached the same level as the heating power and then depleted the stored energy from the confinement region.

This is consistent with the diamagnetic loop measurement, which shows correspondingly that the diamagnetic energy dropped once P_{rad} approached the heating power, and is further supported by a limiter IR camera, which shows a strongly reduced power load on the limiter in the plasma collapse phase [14].

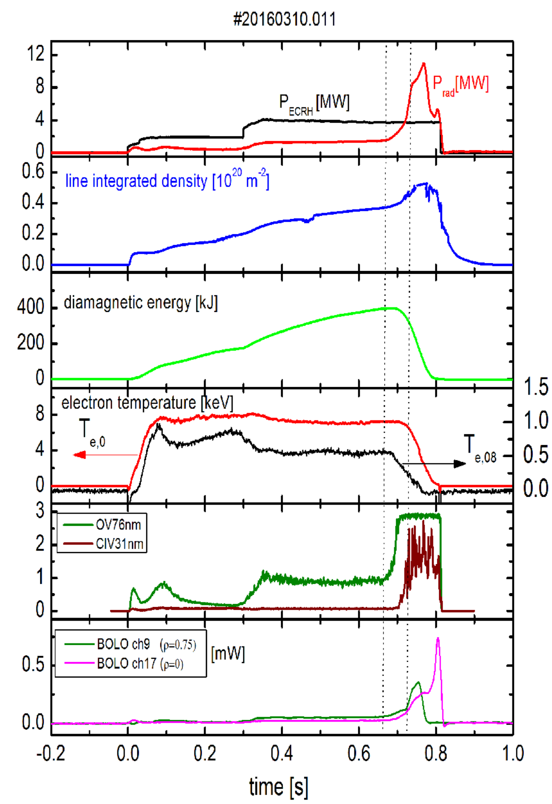

Fig. 5. Time traces of a typical H_2 discharge terminated by radiation (collapse starting at 0.68 s). From top to bottom: ECRH power and total radiated power, line-integrated plasma density, diamagnetic energy, electron temperatures at the center and edge, the spectroscopic signals from O V and C IV, and bolometer signals of two channels viewing central and edge plasma regions. The first dashed vertical line indicates the time point when the O V emission increases and the edge T_e ($\rho = 0.85$) decreases, while the second indicates the time point when the central T_e begins to drop.

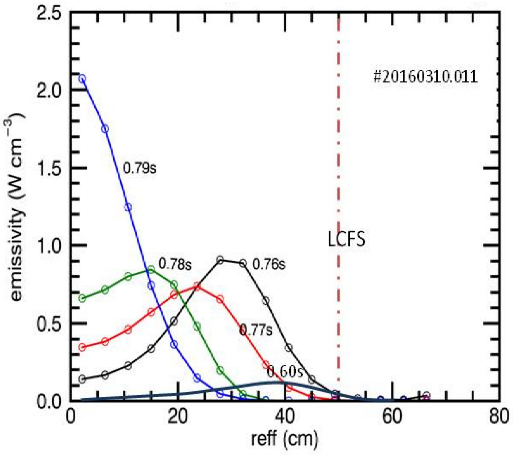

Fig. 6. 1D emission profiles obtained by Abel-inversion of the horizontal bolometer line integrals in discharge #20160310.011 for the flattop phase (t = 0.6 s) and during radiative collapse (t = 0.76–0.79 s). The profile peak moves inward when plasma collapses.

Radiation profiles

Assuming constant emissivity on the magnetic flux surface, a 1D emissivity profile can be deduced from the bolometer line integrals by means of Abel inversion. The resulting profiles are shown in Fig. 6, which shows the profile evolution for discharge #20160310.011 during the collapse phase from 0.76 s to 0.79 s indicated by the two vertical dashed lines in Fig. 5, using $t = 0.6$ s as reference. At $t = 0.6$ s before the second gas-puffing, the emission profile is peaked at ρ ~ 0.8. During the collapse process, the peak shifts inward and eventually reaches the plasma center leading to termination of the discharge.

The LoS of the bolometer channels in both HBC and VBC allow for a tomographic reconstruction of a 2D radiation distribution. Using a similar discharge [15] (#20160309.007 to #20160310.011) as an example, we show how the radiation distribution shrinks in 2D space when the plasma begins to collapse. The inversion is based on the Gaussian Process Tomography (GPT) method [16] and carried out within the Minerva framework [17]. The results are shown in Fig. 7, including a time point $t = 0.5$ s prior to onset of the thermal instability, and two later time points during the collapse process. The poloidal asymmetries in radiation are not yet understood.

The radiative power loss factor

The total radiation under different plasma conditions has been investigated for hydrogen plasmas. Figure 8 shows the radiation loss fraction $f_{rad} = P_{rad}/P_{ECRH}$ as a function of line-averaged density $\langle n_e \rangle$ for different heating power levels.

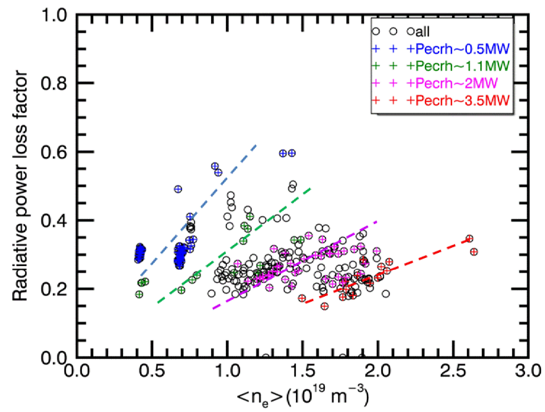

Fig. 8. Radiation loss factor in hydrogen plasmas as a function of line-averaged plasma density at different heating powers (black circles). The discharges are collected from the last week of the first experimental campaign of W7-X. Each point is averaged over a 100-ms quasi-flattop of T_e and $\langle n_e \rangle$. Cross colors indicate different heating powers (blue: 0.5MW, green: 1.1MW, cyan: 2.0MW, red: 3.5MW). The dashed lines are guide to the eye.

The data shown in Fig. 8 are taken from the discharges of the last week of the first experiment campaign. Each point is averaged over a 100-ms quasi-flattop of T_e and line-integrated density. Associated with wall conditioning, the data are scattered in a large range. Even so, they clearly show two tendencies: f_{rad}, for a given heating power,

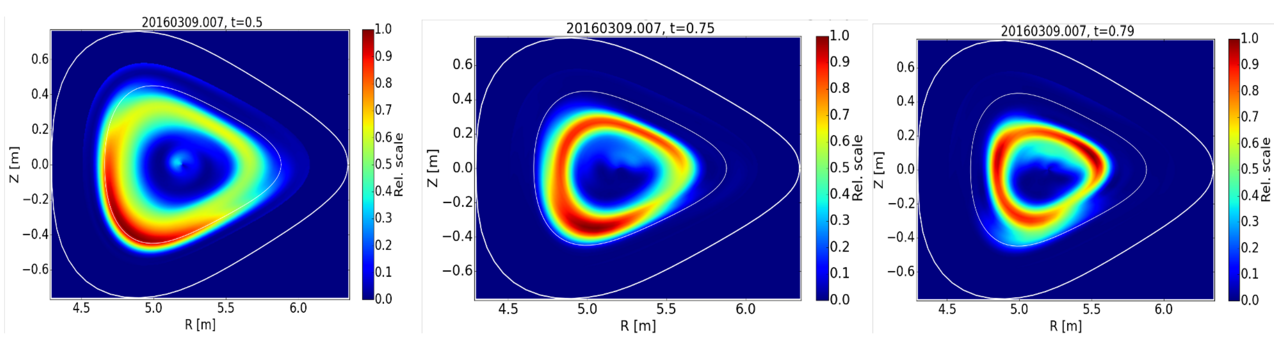

Fig. 7. Tomographic inversion based on bolometer signals for transient phases to radiative collapse in discharge #20160309.007. The inner white line stands for the last closed flux surface defined by the limiter.

increases with line-averaged density $\langle n_e \rangle$, as indicated by the dashed lines, and decreases with increasing heating power for a fixed $\langle n_e \rangle$. For example, for a heating power around 0.5 MW, f_{rad} lies in the range 30–60% (blue) and decreases to 20–40% for 1.1 MW (green) and further drops to 15–35% for higher power levels (2 MW in cyan and 3.5 MW in red). More detailed analysis is under way.

D. Zhang, R. Burhenn, A. Alonso, B. Buttenschön, Y. Feng, L. Giannone, M. Hirsch, U. Höfel, R. Lauber, M. Marquardt, K. Rahbarnia, J. Svensson , G. A. Wurden, R. Brakel, O. Grulke, J. Knauer, R. König, H. Laqua, S. Marsen T. Stange, T. Schröder, H. Thomsen, G.M. Weir, A. Werner and the W7-X Team

Max-Planck Institut für Plasmaphyisk
17491 Greifswald, Germany
E-Mail: daihong.zhang@ipp.mpg.de

References

[1] D. Zhang, L. Giannone, et al., 34th EPS Conference On Plasma Phy., Warsaw, Poland (2007).

[2] T. Klinger et al., Plasma Phys. Contr. Fusion **59**, 1 (2017).

[3] K. F. Mast et al., Rev. Sci. Instrum. **62**, 744 (1991).

[4] L. Giannone, K. Mast, and M. Schubert, Rev. Sci. Instrum. **73**, 3205 (2002).

[5] D. Zhang et al., Rev. Sci. Instrum. **81**, 10E134 (2010).

[6] S. Ullrich, H. J. Hartfuss, M. Hirsch, H. Laqua, *Stellarator News* Issue 98, 2005.

[7] D. Zhang et al., 38th EPS Conf. on Contr. Fusion and Plasma Phys., Strasbourg, P5.056 (2011).
B. Buttenschön et al., P4.012 in Proc. 43rd EPS Conf. Plasma Phys. Contr. Fusion, Leuven, Belgium (2016).

[8] H. Thomsen et al., J. Instrum. **10**, P10015 (2015).

[9] S. Marsen et al. in Proc. 43th EPS Conference Plasma Physics, Leuven, Belgium, P4.002 (2016).

[10] M. Hirsch et al., in Proc. 43th EPS Conference Plasma Physics, Leuven, Belgium, P4.007 (2016).

[11] P. Kornejew et al. to be published; J. Knauer, et al., 43th EPS Conference On Plasma Physics, Leuven, Belgium, P4.017.

[12] K. Rahbarnia et al., in Proc. 43th EPS Conference Plasma Physics, Leuven, Belgium, P4.011 (2016).

[13] T. Wauters et al., in Proc. 40th EPS Conference Plasma Physics, Leuven, Belgium, (2016).

[14] G. A. Wurden et al., Rev. Sci. Instrum. 2016.

[15] D. Zhang et al., in Proc. 43th EPS Conference Plasma Physics, Leuven, Belgium, P4.015 (2016).

[16] J. Svensson, Nonparametric Tomography using Gaussian Processes, JET Internal Report EFDA-JET-PR(11)24, 2011.

[17] J. Svensson, A. Werner, "Large Scale Bayesian Data Analysis for Nuclear Fusion Experiments," In Proc. IEEE Workshop on Intelligent Signal Processing (WISP) 2007.